Strain Effects on Ballistic Current in Ultrathin DG SOI MOSFETs

Hideki Minari and Nobuya Mori
Division of Electrical, Electronic and Information Engineering
Graduate School of Engineering, Osaka University
2–1 Yamada-oka, Suita City, Osaka 565-0871, Japan
Email: minari@e3.eei.eng.osaka-u.ac.jp

***Abstract*—Atomistic electron transport simulation based on a nonequilibrium Green's function method and a tight-binding approximation has been performed for $\langle 110 \rangle$-channel strained Si ultrathin double-gate silicon-on-insulator MOSFETs on a (100) substrate. Simulation results show that the tensile strain enhances the ballistic current, while the compressive strain gives opposite results.**

***Keywords*—Silicon; Strain; MOSFET; NEGF method; Tight-binding; Simulation**

I. Introduction

In ultra-small silicon metal-oxide-semiconductor field-effect transistors (MOSFETs), quantum mechanical effects, such as direct source-to-drain tunneling, subband quantization along the gate confining direction, and gate leakage current, significantly affect the transport characteristics, which may prevent further device scaling. To overcome the difficulties associated with conventional device scaling, MOSFETs utilizing new materials and new geometrical structures have been extensively studied. MOSFETs with strained Si channels are considered to be one of most promising device structures in the sub-$100\,\mathrm{nm}$ regime [1].

To design ultra-small strained Si MOSFETs, a quantum-mechanical device simulator which can handle strained materials with atomic resolution is strongly needed. The nonequilibrium Green's function (NEGF) method allows us to calculate quantum transport characteristics in MOSFETs [2]–[5]. By combining the NEGF method with an empirical tight-binding (TB) approximation, quantum-mechanical computations with atomic resolution can be achieved [4].

In our previous study, we performed one-dimensional simulation of Si n-i-n structures to study strain effects on ballistic and Zener tunneling current [6], [7], and two-dimensional simulation of ultrathin double-gate (DG) silicon-on-insulator (SOI) MOSFETs to study crystalline orientation effects on ballistic hole current [8]. In the present study, we have performed two-dimensional simulation of electron transport in n-type strained Si DG SOI MOSFETs. We especially focus on strain effects on the ballistic electron current in $\langle 110 \rangle$-channel devices on a (100) substrate.

II. Simulation Method

We consider n-type DG SOI MOSFETs with a gate-length of $15\,\mathrm{nm}$, Si-body thickness of $3\,\mathrm{nm}$, and SiO_2 thicknesses of $1\,\mathrm{nm}$ (see Fig. 1). The current flows along the x-direction (parallel to a $\langle 110 \rangle$ crystalline axis). The confining direction is chosen to be along the z-direction (parallel to a $\langle 100 \rangle$ crystalline axis). The device is assumed to have an infinite width in the y-direction (parallel to a $\langle 110 \rangle$ crystalline axis). The doping concentration in the source and drain regions, each of which is $7\,\mathrm{nm}$ long, is $1 \times 10^{20}\,\mathrm{cm}^{-3}$. The gates are assumed to consist of a mid-gap metal.

We calculated ballistic electron current using the NEGF method [2]. For the x- and z-directions, we use a discrete lattice in real space. For the y-direction, we assume periodic boundary conditions and use the eigenstate basis labeled by wavevector k_y. We discretize the k_y-space into meshes and evaluate the spectral function, $A(k_y, E)$, and transmission function, $T(k_y, E)$, at each mesh point. Carrier density and the total transmission function are then calculated by summing these functions over k_y- and energy spaces. In the present study, we neglect scattering and assume ballistic transport.

We take into account the full-band structure and strain effects within an empirical $sp^3d^5s^*$ nearest-neighbor TB approximation [9], [10]. The $sp^3d^5s^*$ TB approximation includes ten orbitals without the spin-orbit coupling. Strain effects can be included by scaling the TB matrix elements with respect to the strain tensor and bond-length changes [9]. The dependence

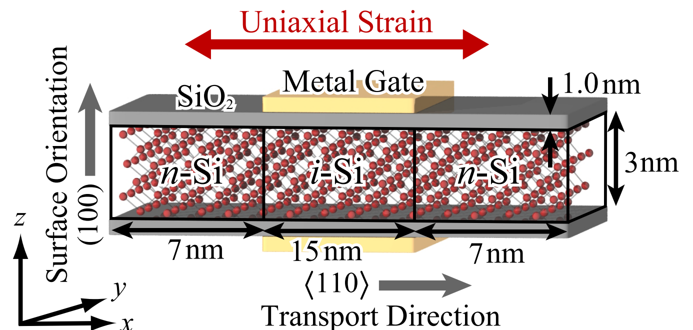

Fig. 1. Schematic diagram of the $\langle 110 \rangle$-channel strained Si ultrathin double-gate silicon-on-insulator MOSFET on a (100) substrate. We define the x- and z-direction as the source-to-drain transport and gate confining direction, respectively. We consider three cases; (a) no strain, (b) -1% uniaxial compressive strain and (c) $+1\%$ uniaxial tensile strain along the x-axis.

978-1-4244-1753-7/08/$25.00 ©2008 IEEE

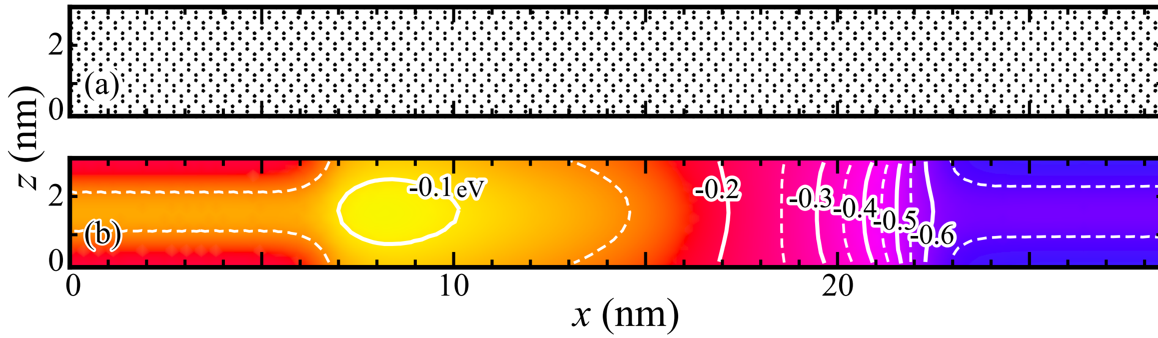

Fig. 3. (a) Si atomic positions in the calculation domain. (b) Potential profile of the device without strain.

of the two-center integral $ij\kappa$ on bond length is considered using a generalized version of Harrison's d^{-2} law,

$$ij\kappa(d) = ij\kappa(d_0)\left(\frac{d_0}{d}\right)^{n_{ij\kappa}} \quad (1)$$

where d (d_0) is the strained (unstrained) interatomic distance, and $n_{ij\kappa}$ represents empirical parameters of the orbital-dependent exponents [9]. The effects of a tetragonal crystal field induced by uniaxial $\langle 100\rangle$ strain are included assuming a linear dependence of the on-site energies of the d states on the strain tensor [9]. Figure 2 shows the lowest subband dispersion of a $3\,\mathrm{nm}$-thick unstrained Si quantum well in (k_x, k_y)-space calculated within the TB approximation. 4-fold valleys locate diagonally (we call them "*diagonal valley*" hereafter), while 2-fold valleys locate at $k_x = k_y = 0$ (we call them "*gamma valley*"). Note that the transport direction is along a $\langle 110\rangle$ direction in the present study.

We investigate three cases; (a) no strain, (b) -1% uniaxial compressive strain and (c) $+1\%$ uniaxial tensile strain along the x-axis. We used a macroscopic elastic theory [11] to evaluate the lattice constants along the y- and z-directions. We treat the Si/SiO_2 interfaces with the H termination model of Lee [12] to eliminate the artificial surface states in the energy region of interest.

III. Results and Discussion

Black dots in Fig. 3(a) show the Si atomic positions; We considered 1,650 atoms in the calculation domain. Figure 3(b) shows the potential profile of the device without strain at drain voltage $V_\mathrm{d} = 0.5\,\mathrm{V}$, gate voltage $V_\mathrm{g} = 0.8\,\mathrm{V}$, and $T = 300\,\mathrm{K}$. Darker areas correspond to lower potential regions. The potential profiles are obtained through a self-consistent solution of Poisson and NEGF equations.

Current density spectra are plotted in Fig. 4. The integrated current density is $1.1 \times 10^3\,\mu\mathrm{A}/\mu\mathrm{m}$ for no strain, $7.2 \times 10^2\,\mu\mathrm{A}/\mu\mathrm{m}$ for -1% uniaxial compressive strain, and $2.1 \times 10^3\,\mu\mathrm{A}/\mu\mathrm{m}$ for $+1\%$ uniaxial tensile strain. We find that the tensile strain enhances the ballistic electron current, while the compressive strain gives opposite results. This can be

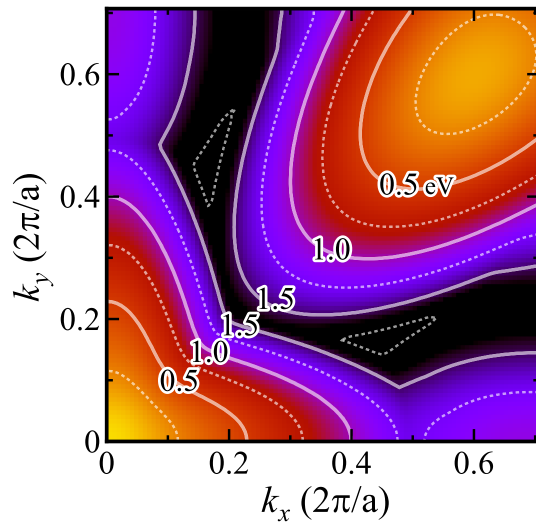

Fig. 2. The lowest subband dispersion of a $3\,\mathrm{nm}$-thick unstrained Si quantum well in (k_x, k_y)-space. 4-fold valleys locate diagonally (*diagonal valley*), while 2-fold valleys locate at $k_x = k_y = 0$ (*gamma valley*).

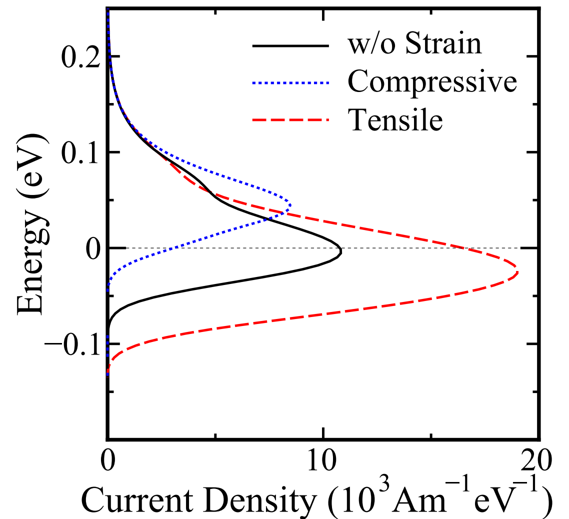

Fig. 4. Current density spectra for unstrain (solid line), -1% uniaxial compressive strain (dotted line), and $+1\%$ uniaxial tensile strain (dashed line). The energy zero is chosen to be the Fermi level in the source contact.

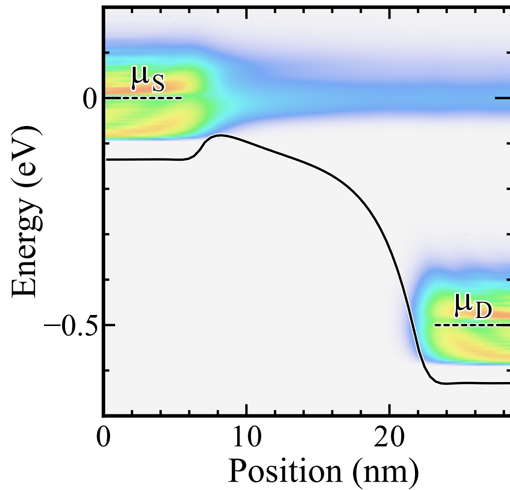

Fig. 5. Electron density spectra (density plot) for the device without strain. Solid line shows the potential profiles and dashed lines indicate the Fermi levels in the source (μ_S) and drain (μ_D) contacts.

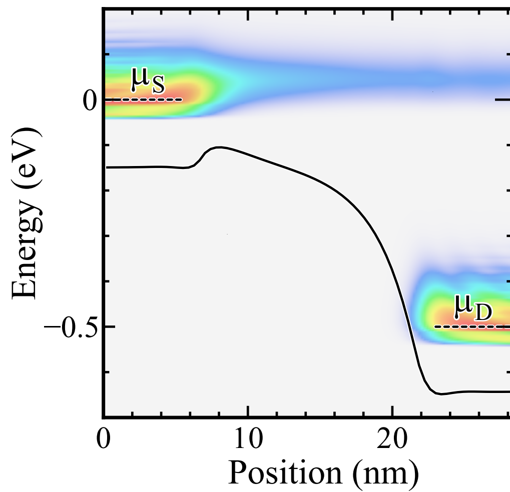

Fig. 6. The same as Fig. 5 but under -1% uniaxial compressive strain.

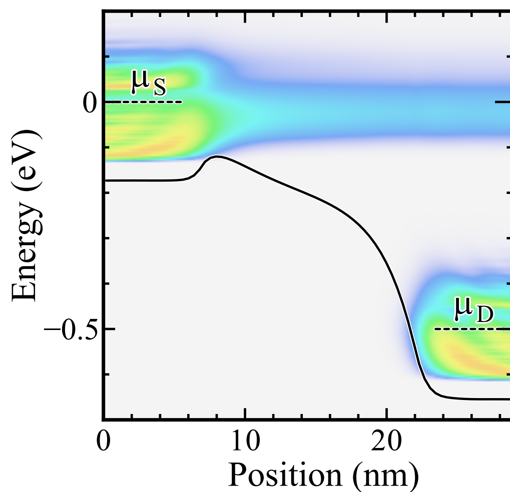

Fig. 7. The same as Fig. 5 but under $+1\%$ uniaxial tensile strain.

understood by considering the difference in the strain-induced energy shift as will be explained in the following.

Figures 5, 6, and 7 show the electron density spectra of no strain, compressive strain, and tensile strain devices, respectively. Solid lines show the potential profile along the center of the device. The energy zero is chosen to be the Fermi level in the source contact. We see that electron distribution in energy space is wider in the tensile strain device. This is because that the energy separation, ΔE, between the 2-fold *gamma valley* and the 4-fold *diagonal valley* becomes larger in the tensile device (see Figs 8, 9, and 10). The energy separation between the potential profile and the bottom of the density spectra in the contact regions reflects the subband confining energy, and we see that the confining energy of the compressive strain device is larger than that of the tensile strain device.

Figures 8, 9, and 10 show the wavevector resolved density-of-states for no strain, compressive, and tensile strain devices. The *gamma valley* has lighter effective mass along the transport direction compared to the *diagonal valley*. Electrons in the *gamma valley* mainly contribute to current under tensile strain, because the energy separation, ΔE, between the *gamma valley* and the *diagonal valley* is large. This results in the enhancement of the ballistic electron current. On the other hand, under compressive strain both the *gamma valley* and *diagonal valley* contribute to current and an average effective mass becomes heavier leading to the reduction of the ballistic electron current.

IV. Conclusion

We performed atomistic transport simulation based on the NEGF method and the empirical $sp^3d^5s^*$ nearest-neighbor TB approximation for $\langle 110 \rangle$-channel strained Si ultrathin DG SOI MOSFETs on a (100) substrate. We find that the tensile strain enhances the ballistic current, while the compressive strain gives opposite results. This can be understood by considering the difference in the strain-induced energy shift.

Acknowledgment

The authors gratefully acknowledge useful and insightful discussion with Hideki Oka, Kiyoshi Ishikawa, Hiroshi Takeda, and Shinya Yamakawa. This work was supported by the Semiconductor Technology Academic Research Center (STARC) and the Global COE Program "Center for Electronic Devices Innovation" (CEDI).

References

[1] S. Takagi, T. Mizuno, T. Tezuka, N. Sugiyama, S. Nakaharai, T. Numata, J. Koga, and K. Uchida, *Solid-State Electron.*, **49**, 684 (2005).
[2] S. Datta, *Electronic Transport in Mesoscopic Systems*, (Cambridge University Press, Cambridge, UK, 1995).
[3] H. Haug and A.-P. Jauho, *Quantum Kinetics in Transport and Optics of Semiconductors* (Springer, Berlin, 1996).
[4] A. Pecchia and A. Di Carlo, *Rep. Prog. Phys.*, **67** 1497 (2004).
[5] M. Lundstrom and J. Guo, *Nanoscale Transistors: Device Physics, Modeling, and Simulation* (Springer, New York, 2006).
[6] H. Minari and N. Mori, *Jpn. J. Appl. Phys.*, **46**, 2076 (2007).

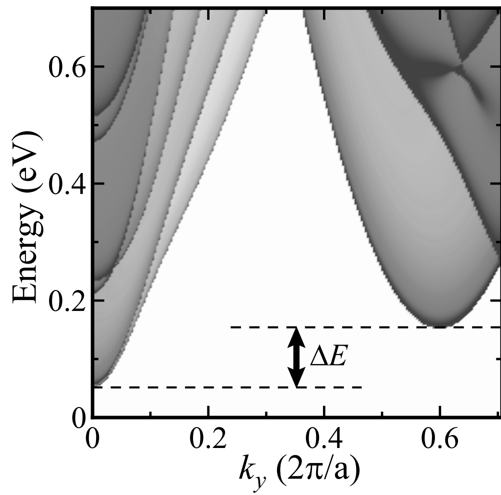

Fig. 8. Wavevector resolved density-of-states of the device without strain. Dashed lines show the lowest energy of the *gamma valley* and that of the *diagonal valley*.

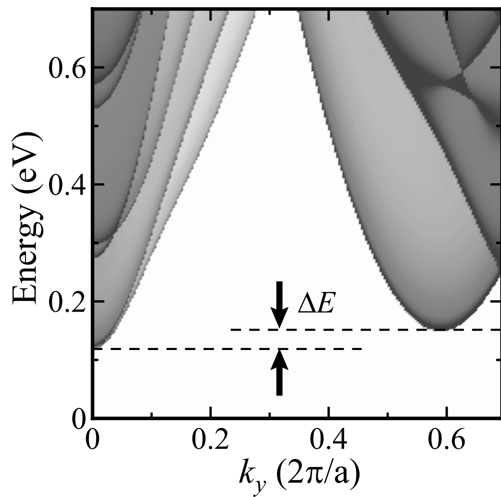

Fig. 9. The same as Fig. 8 but under -1% uniaxial compressive strain.

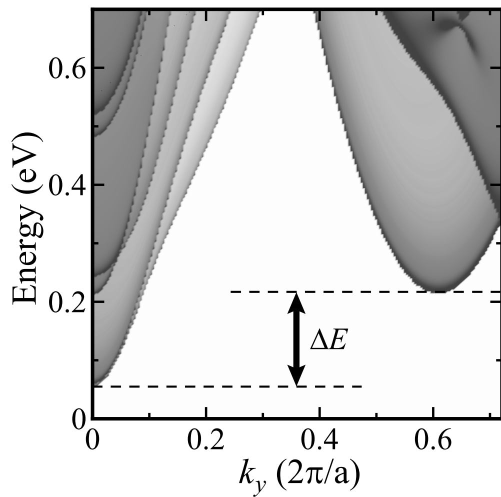

Fig. 10. The same as Fig. 8 but under $+1\%$ uniaxial tensile strain.

[7] H. Minari and N. Mori, *Jpn. J. Appl. Phys.*, **47**, 2621 (2008).

[8] H. Minari and N. Mori, *Simulation of Semiconductor Processes and Devices Vol. 12* (edited by T. Grasser and S. Selberherr), pp. 229-232 (2007).

[9] J.-M. Jancu, R. Scholz, F. Beltram, and F. Bassani, *Phys. Rev. B*, **57**, 6493 (1998).

[10] A. V. Podolskiy and P. Vogl, *Phys. Rev. B*, **69**, 233101 (2004).

[11] C. G. V. de Walle, *Phys. Rev. B*, **39**, 1871 (1989).

[12] S. Lee, F. Oyafuso, P. von Allmen, and G. Klimeck, *Phys. Rev. B*, **69**, 045316 (2004).